Cross sections for low-energy inelastic H + Na collisions

A. K. Belyaev
Department of Theoretical Physics, Herzen University, St. Petersburg 191186, Russia

P. S. Barklem
Department of Physics and Astronomy, Uppsala University, Box 516, S-75120 Uppsala, Sweden

A. S. Dickinson
School of Chemistry, Newcastle University, Newcastle upon Tyne NE1 7RU, United Kingdom

F. X. Gadéa
Laboratoire de Chimie et Physique Quantique, CNRS UMR 5626, Institut de Recherche sur les Systèmes Atomiques et Moléculaires Complexes, Université Paul Sabatier, 118 Route de Narbonne, F-31062 Toulouse, France
(Received 20 January 2010; published 24 March 2010)

Full quantum-scattering calculations are reported for low-energy near-threshold inelastic collision cross sections for H + Na. The calculations include transitions between all levels up to and including the ionic state (ion-pair production) for collision energies from the threshold up to 10 eV. These results are important for astrophysical modeling of spectra in stellar atmospheres. Results for the $3s$-$3p$ excitation are carefully examined using three different quantum chemistry input data sets, and large differences are found near the threshold. The differences are found to be predominantly due to differences in the radial coupling rather than potentials and are also found not to relate to differences in couplings in a simple manner. In fact, of the three input couplings, the two that are most similar give the cross sections with the largest differences. The $3s$-$3p$ cross sections show orbiting resonances which have been seen in earlier studies, while Feshbach resonances associated with closed channels were also found to be present in the low-energy cross sections for some transitions.

DOI: 10.1103/PhysRevA.81.032706 PACS number(s): 34.50.Fa

I. INTRODUCTION

The measurement of abundances of chemical elements in stellar atmospheres, as interpreted from stellar spectra, is of fundamental importance in modern astrophysics. Inelastic collision processes in the stellar atmosphere where the spectrum is formed are important in determining properties of the nonequilibrium gas and these properties must be known in order to interpret such spectra accurately. In the atmospheres of hot ($\gtrsim$7500 K) stars where hydrogen is ionized, the collision processes are dominated by electrons. However, in cooler (around 4000–7500 K) F-, G-, and K-type stars like the sun, collisions with neutral hydrogen atoms could become important due to their sheer number, as atoms typically outnumber electrons by around four orders of magnitude in regions where the spectral lines are formed. In old, metal-poor stars of similar temperature, which are particularly important for understanding the very early stages of the universe, atoms can outnumber electrons by a couple more orders of magnitude. For atmospheres of these temperatures, $kT \approx 0.2$–0.6 eV for both neutrals and electrons, characteristic collision energies are comparable to typical atomic transition energies, and thus low-energy near-threshold collisions are most important.

The possible importance of collisions with neutral hydrogen was first pointed out by Steenbock and Holweger [1] in the context of their study of the nonequilibrium formation of the spectral lines of Li. This led to an experimental study [2] of $H + Na(3s) \rightarrow H + Na(3p)$ at low energies (15–1500 eV), though not down to the threshold due to experimental difficulties. They compared the measurements with Landau-Zener model predictions and from the general agreement concluded that the essential mechanism was the nonadiabatic transition associated with the avoided ionic crossing. Revised experimental data, including results down to 10 eV, were presented in [3].

This work has been followed by a number of theoretical studies involving some of the present authors. First, quantum-scattering calculations were performed for $H + Na(3s) \rightarrow H + Na(3p, 4s)$ down to the threshold [3] and good agreement with the experimental results was found. However, the calculations showed that while the Landau-Zener model provides a reasonable description of the coupling mechanism at collision energies above 10 eV, it fails at lower energies. At these lower energies, which are most relevant for stellar-atmosphere applications, the cross sections were calculated to be several orders of magnitude higher than those predicted by the Landau-Zener model. It was also concluded that the precision of the quantum-chemical data, particularly the nonadiabatic radial-coupling data, was the stumbling block before highly reliable calculations of the cross sections near the threshold could be calculated.

This work on H + Na was followed by calculations for H + Li [4] where for the lowest four states a full quantum-scattering treatment was used, whereas for the remaining six higher states, up to and including the ionic limit, order-of-magnitude estimates were made using a multichannel Landau-Zener model. These calculations were based on quantum-chemical data calculated by some of the present authors [5]. This was followed by astrophysical application [6], where it was found that direct excitation collisions $H + Li(nl) \rightarrow H + Li(n'l')$ were unimportant, yet the ion-pair production and mutual

neutralization process $H + Li(3s) \rightleftharpoons H^- + Li^+$ was found to be rather important, resulting in changes in spectral line strengths of around 20% in cool, metal-poor, subgiant stars.

In this paper we revisit low-energy H + Na collisions, because data for transitions between all possible Na levels are needed for astrophysical modeling, while the earlier experimental and theoretical studies dealt primarily with the resonance transition. We concentrate on the transitions in the singlet system of NaH because the presence of an ionic channel causes cross sections in the singlet system to dominate those in the triplet. Singlet low-energy H + Na collisions are also of interest as a standard benchmark case, since a number of sets of quantum-chemical data are available, allowing us to study in more detail the sensitivity of these very small near-threshold cross sections to the potentials and couplings from different calculations. Recent work [7] has demonstrated that, for the $3s$-$3p$ excitation, the singlet results near the threshold can differ markedly due to small differences in the nonadiabatic radial coupling.

II. QUANTUM-CHEMICAL DATA

This study of inelastic Na + H collision processes is carried out in the framework of the standard Born-Oppenheimer approach. The problem is treated in two steps: (i) the quantum-chemical fixed-nuclei electronic structure calculations and (ii) the nonadiabatic nuclear dynamics. The treatment can be performed in the adiabatic, the diabatic, or the hybrid (mixed diabatic-adiabatic) representations. All three representations are used in this paper. The quantum-chemical calculations result either in adiabatic potentials and nonadiabatic couplings or in a diabatic Hamiltonian matrix, depending on the representation used. Although the low-lying NaH adiabatic $^1\Sigma^+$ potentials have been calculated in many papers, the number of complete sets of quantum-chemical data is very limited. The available potentials and couplings are discussed in the next section.

A. Available potentials with couplings

Three sets of quantum-chemical data, including nonadiabatic couplings for the singlet NaH system, have been used in this work:

1. Pseudopotential calculations with two active electrons. For the lowest ten $^1\Sigma^+$ states, these are described by Dickinson *et al.* [8]. The wave functions have been transformed from the adiabatic representation to a diabatic representation, which is discussed further in Sec. II B. Adiabatic and diabatic potentials were calculated for these ten $^1\Sigma^+$ states, along with the diabatic Hamiltonian matrix.

2. *Ab initio* calculations using the multireference single- and double-excitation configuration-interaction (MRD-CI) method. Adiabatic potentials for the X, A, and $C\,^1\Sigma^+$ states, $B\,^1\Pi$ state, a, c, and $d\,^3\Sigma^+$ states, and the $b\,^3\Pi$ state were obtained, as well as all radial and rotational couplings between them [3].

3. *Ab initio* calculations using a full-valence complete active-space self-consistent field, followed by a multireference configuration-interaction (MRCI) calculation. The radial coupling between the X and $A\,^1\Sigma^+$ states was obtained, along with the corresponding adiabatic potentials [7].

The pseudopotential calculations have the advantage of covering the largest number of states, namely, all $^1\Sigma^+$ states up to and including the ionic state. As discussed in the introduction, this wide coverage is vital for astrophysical application. Spectroscopic results calculated using these X and A potentials compare very well with experimental data (see Sec. II C).

On the other hand, inelastic cross sections, which are the main interest of this paper, are determined primarily by the nonadiabatic couplings, rather than the potentials. The strength of both the MRD-CI and the MRCI data is that they both have been obtained by *ab initio* methods and have neither adjustment nor smoothing except for smooth corrections in the asymptotic region ($R > 20a_0$, where R denotes the internuclear separation), in particular, to obtain correct dissociation limits. The MRD-CI calculations have been used, along with triplet calculations, in previous work [3] and the resulting cross sections for $3p$ and $4s$ excitation yield reasonable agreement with the measurements, which are available for energies between 10 and 600 eV [3].

The MRCI calculation was intended primarily to provide an independent check on the X-A radial coupling and was performed in the range $R = (1.5\text{–}12)a_0$ [7]. It was shown that at low collision energies even a slight variation of a nonadiabatic coupling can change an inelastic cross section by more than an order of magnitude. For these reasons, several sets of quantum-chemical data have been used in this paper to compare the data and the resulting cross sections from the different quantum-chemical calculations.

B. Adiabatic and diabatic potentials and couplings

Figure 1 compares the adiabatic potentials from the three quantum-chemical calculations for $^1\Sigma^+$ symmetry. Recently large quantum-chemical calculations for the $X\,^1\Sigma^+$ state have been performed [9] by using the coupled-cluster theory with single, double, and perturbative triple excitations [CCSD(T)]. This potential is also shown and assumed to be the most reliable calculation presently available.

The series of avoided crossings associated with the ionic state is clearly apparent. It is these avoided crossings, and their associated nonadiabatic radial couplings, which provide the dominant mechanism for transitions at low energy. In this work we study cross sections within about 10 eV of threshold as being the most relevant to astrophysical applications and complementing the experimental work at higher energies. We thus require quantum-chemical data in this symmetry.

1. Pseudopotential calculations

Dickinson *et al.* [8] derived the lowest ten $^1\Sigma^+$ state adiabatic NaH potentials using a pseudopotential method with two active electrons. They then derived the 10×10 diabatic Hamiltonian matrix (H_{ij}) using the method of [10], taking the electronic origin on the Na nucleus. This method uses an effective metric for the overlap matrix, which corresponds to a static substitute of the electron translation factors and ensures,

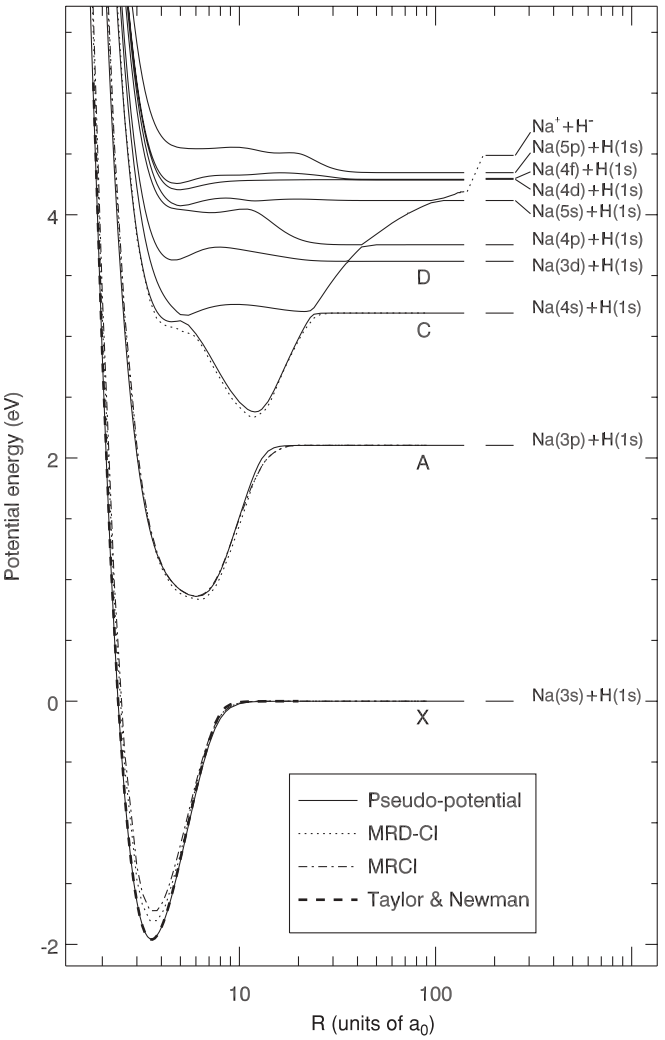

FIG. 1. Adiabatic potentials for the lowest ten $^1\Sigma^+$ states of the NaH quasimolecule obtained using different quantum-chemical calculations. MRCI values are only available for the X and A states for $R \lesssim 12a_0$, and MRD-CI values for the X, A, and C states. The atomic states and energies at dissociation are shown in the right-hand side of the figure. The pseudopotential calculations extend to $316a_0$. The dashed line plots the *ab initio* X-state potential from [9].

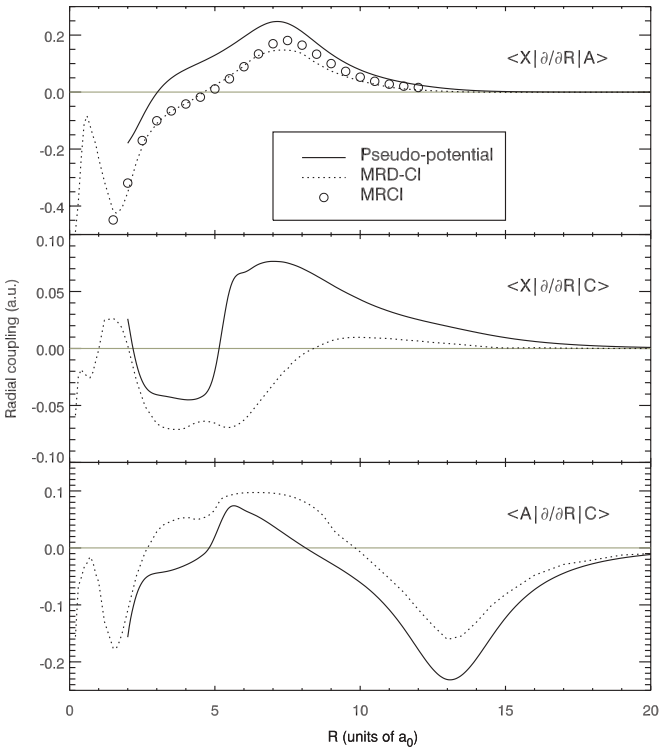

FIG. 2. Plot comparing radial couplings between the lowest three $^1\Sigma^+$ states. Note the differing scales on the y axis. The data are calculated using different electronic origins; however, as discussed in the text, this explains differences of only about 0.01 a.u.

at large distances, that the transformation between the adiabatic and diabatic representations is simply the identity matrix. This approach was shown to give good results compared to various other methods [11]. The derived ionic diabatic curve was corrected for the underestimate of the H^- electron affinity and this corrected diabatic matrix was diagonalized to yield the final adiabatic results. This diagonalization yielded the transformation matrices.

Nonadiabatic couplings were derived from these singlet adiabatic and diabatic results and transformation matrix using both the numerical differentiation and the Hellmann-Feynman (HF) expressions of [12]. Because the HF expressions involve numerical differentiation of the Hamiltonian matrices only, which vary more smoothly than the transformation matrices, the HF results are expected to be more reliable.

The results from both methods were, however, in quite good agreement. The nonadiabatic radial couplings between the three lowest $^1\Sigma^+$ states are plotted in Fig. 2.

To help assess the importance of transformations between adiabatic and diabatic bases, we have generated a new diabatic matrix from these adiabatic potentials and nonadiabatic couplings using the standard method of [13]. It proved necessary to start the inward integration at $41a_0$ because using larger R values led to difficulties at the outer avoided crossings, which in turn led to poor results at small distances for some channels. These difficulties were attributed to the use of insufficient points to define the outer crossings precisely in the original diabatic calculation. (Unfortunately it was no longer possible to extend the original calculations.) Having the electronic origin at Na in the pseudopotential calculation provides zero radial couplings in the asymptotic region, which simplifies the application of the Smith diabatization procedure.

These diabatic potentials from the HF nonadiabatic couplings are compared in Fig. 3 to the original diabatic potentials from [8]. While there are some small differences around the minima in some channels, the positions of the crossings are well reproduced. The couplings between the lowest four states (not shown) are also generally well reproduced, particularly the critical coupling for the $3s$-$3p$ transition. Diabatic potentials derived using the nonadiabatic couplings obtained by differentiating the transformation matrix were in almost as good agreement with the original calculations [8], but the couplings were in distinctly poorer agreement.

Since this transformation from diabatic to adiabatic and back to diabatic almost regains the original diabatic matrix,

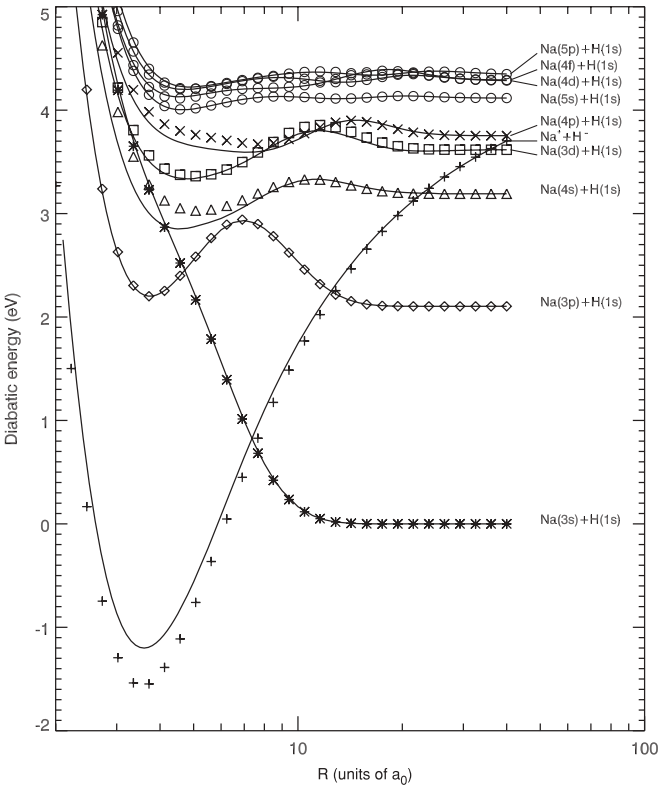

FIG. 3. Comparison of original diabatic potential results of [8] (points) with HF diabatic results (solid lines). The Na term at dissociation is indicated.

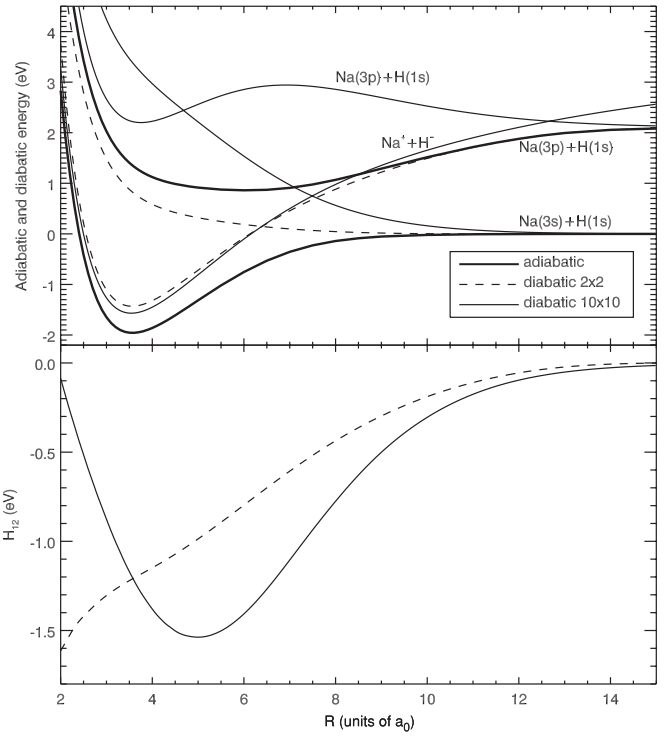

FIG. 4. Comparison of ten-state [8] and two-state diabatic potentials and couplings. Adiabatic potentials are also shown. The key is the same for both panels.

it appears that the original singlet diabatic matrices, derived using the method of [10], are reliable. These matrices, together with the assumption of negligible residual radial couplings, provide not only the adiabatic potentials (see, e.g., Fig. 1) but also the nonadiabatic couplings (Fig. 2).

Two-state diabatic Hamiltonian. It is worth emphasizing that the position of the maximum of the X-A pseudopotential nonadiabatic coupling, $7.15a_0$ (see Fig. 2), differs from the crossing of the corresponding ten-state diabatic potentials, $7.83a_0$ [8] (see Fig. 3). To clarify the situation, using the method of [13] we have generated a new 2×2 diabatic matrix from the X and A adiabatic potentials and the X-A nonadiabatic derivative coupling derived from the full pseudopotential calculation. The 2×2 diabatic potentials and the off-diagonal matrix element are shown in Fig. 4, together with the relevant matrix elements from the 10×10 diabatic Hamiltonian matrix.

As the pseudopotential nonadiabatic radial coupling is close to Lorentzian in form, the 2×2 diabatic potentials cross, indicating that the broad nonadiabatic region around $R \approx 3$–$9a_0$ (see Fig. 2) is the avoided crossing of two physically meaningful molecular states: the ionic state and the covalent state. It is clearly seen in Fig. 4 that the $3p$ diabatic potential derived in the two-state approximation and the ionic potential from the ten-state representation nearly coincide, apart from in the internuclear distance range $R > 12a_0$, where other avoided crossings are located. The covalent molecular state, however, is associated with a single atomic state, $\mathrm{Na}(3s) + \mathrm{H}$, only at large internuclear distances, $R > 11a_0$, and at the distances of interest this covalent molecular state represents a strong mixing of different atomic states, at least the $\mathrm{Na}(3s) + \mathrm{H}$ and $\mathrm{Na}(3p) + \mathrm{H}$ states (see Fig. 4). This results in a significant deviation of the two-state $3s$ diabatic potential from the ten-state $3s$ diabatic potential and in the crossings of the ten-state and the two-state diabatic potentials having different locations. Consequently, the corresponding off-diagonal matrix elements differ by approximately a factor of 2 in the ten-state and two-state representations (see the bottom panel of Fig. 4). In order to estimate parameters for the transition probability using the Landau-Zener (LZ) model, one needs to use the two-state representation. For higher-lying avoided crossings, deviations between the appropriate two-state and the ten-state representations become smaller as the avoided crossings become more localized.

Figure 4 clearly shows that the ten-state $\mathrm{Na}(3s) + \mathrm{H}$ and $\mathrm{Na}(3p) + \mathrm{H}$ diabatic potentials cross each other at $R \approx 5a_0$. Consequently the contributions of the $\mathrm{Na}(3s) + \mathrm{H}$ and $\mathrm{Na}(3p) + \mathrm{H}$ diabatic wave functions to the A-state adiabatic molecular wave function are interchanged for internuclear separations either side of $R \approx 5a_0$. This interchange should be reflected in the X-A nonadiabatic coupling matrix element. Indeed the X-A coupling deviates substantially from Lorentzian form at short internuclear distances, $R \lesssim 5a_0$, even changing sign, which is confirmed by the *ab initio* nonadiabatic coupling calculations (see Fig. 2). This variation of the X-A radial coupling significantly affects the low-energy $3s$-$3p$ excitation cross section.

2. *Ab initio calculations*

The adiabatic potentials calculated by means of the *ab initio* MRD-CI and MRCI methods are also shown in Fig. 1. The methods are described elsewhere and have been proven to be accurate [14,15], though the accuracy of the results depends on the employed basis. The MRD-CI and MRCI potentials are in reasonable agreement with the pseudopotential calculation [8], with the most accurate quantum-chemical potentials [9,16] and with experimental data [17] (see Sec. II C). In the MRCI calculation, the nonadiabatic first-derivative coupling matrix elements were computed by the finite-difference method with a radial increment of $0.01a_0$.

The nonadiabatic radial couplings between low-lying NaH $^1\Sigma^+$ molecular states derived from the MRD-CI and MRCI calculations are plotted in Fig. 2 and compared with the pseudopotential ones. The results from these three calculations are qualitatively similar. The *ab initio* calculations agree well with each other and with the pseudopotential calculation of [18] [see the short-dashed line in their Fig. 3(a)] but differ quantitatively from the pseudopotential values of [8]. These calculations have used different electronic origins: at Na [8,19] and at the center of nuclear mass (CNM) [7,19]. The standard (and simplest) form of coupled-channel equations for the nuclear dynamics requires nonadiabatic couplings with the electron origin at the CNM [19–21]. Using nonadiabatic couplings with a different electron origin leads to extra terms in the dynamical equations [19,22]. The nonadiabatic couplings with different origins can easily be recalculated via the adiabatic potentials and the transition dipole moment [19,21,22]. Na is much heavier than H, so the CNM is close to the Na nucleus. An estimate shows that for NaH the use of the origin at Na should not affect the couplings by more than 0.01 a.u. and, hence, this effect can be neglected.

The same holds for the asymptotic couplings, many of which must be nonzero but rather small. For example, the X-A radial coupling with the electron origin at the CNM has the asymptotic value of 8.4×10^{-3} a.u. [19], which is small compared with the maximum value of $\approx$0.2 a.u. There are two ways to handle nonzero asymptotic couplings in the dynamical treatment: (i) use the t-matrix method in calculations of transition probabilities [19,21] or (ii) cut nonzero couplings at appropriate distances. Both are used in the present case. Because asymptotic couplings are small, the latter does not affect the cross sections greatly if the cutting of couplings is done at appropriate places. Thus, the principal cause of the differences in the X-A radial couplings seen in Fig. 2 appears not to be the different electron origins but the use of different approaches.

The major nonadiabatic coupling differences are twofold: in the values of maxima (minima) and in positions where couplings change sign. As shown below, both are important for low-energy inelastic cross sections. The X-A coupling is of particular interest. The pseudopotential X-A coupling is close to a Lorentzian form, apart from at $R < 3a_0$ where it changes sign. As is well known, the widely used LZ model provides a Lorentzian form for the derivative coupling. The pseudopotential X-A coupling has a maximum value of 0.249 a.u. at $R = 7.15a_0$, which agrees well with the maximum value of 0.251 a.u. at $R = 7.35a_0$ for the LZ coupling [7] but is larger than the maximum values of both the MRD-CI and the MRCI couplings: 0.148 a.u. at $R = 7.35a_0$ [3] and 0.181 a.u. at $R = 7.45a_0$ [7], respectively (i.e., larger by 70% and 40%, respectively). Adjusting the LZ parameters to best match the pseudopotential coupling could improve the agreement but would not alter the conclusion of our discussion.

The pseudopotential X-A coupling has an area under the positive values close to $\pi/2$ obtained from the LZ form. The areas under the positive values of both the MRD-CI and the MRCI couplings are less than $\pi/4$ using zero asymptotic values of the couplings; otherwise they diverge. This is in agreement with previous conclusions (see, e.g., [3,18]). These smaller areas are the result of both smaller maximum values as compared with the LZ coupling and the rather large values of the position where the couplings change sign, $R \approx 4.6a_0$ for both the MRD-CI and MRCI couplings. As discussed in Sec. II B1, this change of sign is due to mixing of the Na($3s$) + H and the Na($3p$) + H diabatic covalent states. Consistent with the small areas under the *ab initio* X-A couplings, the procedure for generating diabatic 2×2 matrices from the *ab initio* data provides noncrossing diabatic potentials.

It is usually assumed that nonadiabatic couplings with larger areas should lead to greater nonadiabatic transition probabilities and, hence, larger inelastic cross sections. Indeed, while this is generally correct for relatively high-energy collisions, the reverse may be true for low-energy collisions, as shown by [7] and confirmed by the present calculations presented below.

C. Spectroscopic comparisons

In this section we compare the available spectroscopic data for the X and A states with the predictions derived from the three potentials employed: pseudopotential, MRD-CI, and MRCI. In 1991, Stwalley *et al.* [17] reviewed the available spectroscopic data for sodium hydride. These data are available for the X and $A\,^1\Sigma^+$ states only. More recent data for the vibrational levels $6 \leqslant v \leqslant 9$ of the X state and for $2 \leqslant v \leqslant 8$ for the A state are available from [23], and for $12 \leqslant v \leqslant 25$ for the A state from [24].

Additional calculations also exist for the X state, namely the previously mentioned CCSD(T) calculation [9], and another [16] using the MRCI method. Neither calculation studied the A state, although [16] did calculate potentials for the $a\,^3\Sigma^+$, $b\,^3\Pi$, and $B\,^1\Pi$ states.

Values of the dissociation energy and equilibrium separation of the X and A states, along with the electronic energy of the A state, are compared in Table I with experimental and other recent theoretical values. For these properties in all cases the pseudopotential results are the most reliable of the three calculations being considered here.

Using Le Roy's code LEVEL [25], comparisons of the rotationless vibrational spacings and the rotational constants were made where possible for $v \leqslant 18$ for the X state, and for $v \leqslant 25$ for the A state. Regarding the vibrational spacings of the X state, [9] did not list the values but their Fig. 1 shows that their error in the lowest 12 vibrational energies was always less than about 10 cm^{-1}. The X-state potential of [16] compares the next best, followed by the pseudopotential values, both agreeing to better than 20 cm^{-1}. The MRD-CI

TABLE I. Dissociation energy, D_e, and equilibrium separation, R_e, of various NaH potentials for the X and A states of NaH compared with experimental and recent theoretical values. Also compared is the electronic energy, T_e, of the A state.

	Pspot[a]	MRD-CI[b]	MRCI[c]	CCSD(T)[d]	MRCI[e]	Expt[f]
			X			
D_e (cm^{-1})	15 787	14 670	14 004	15 823	15 814	15 900 ±100
R_e (a_0)	3.568	3.652	3.638	3.564	3.567	3.566
			A			
T_e (cm^{-1})	22 730	21 420	20 989			22 713
D_e (cm^{-1})	10 024	10 222	9987			10 143
R_e (a_0)	6.057	6.283	5.991			6.035

[a]Pseudopotential from [8].
[b]From [3].
[c]From [7].
[d]From [9].
[e]From [16].
[f]From [17].

and MRCI results show spacings ranging from 20 to 150 cm^{-1} smaller than experimental values, but typically around 50 cm^{-1}, the MRD-CI results being marginally better than MRCI results.

A similar picture is seen for the rotational constants with the values from [9] agreeing best, followed closely by those of [16] and the pseudopotential results, all agreeing to within typically better than 0.025 cm^{-1}, while for MRD-CI and MRCI the results are typically around 0.1 to 0.2 cm^{-1} smaller, the MRD-CI results again marginally better than the MRCI results.

In the case of the A state, the picture is similar, although the MRD-CI and MRCI perform somewhat better here. For the vibrational spacings the pseudopotential data typically agree to better than a few cm^{-1}, though differing by as much as 20 cm^{-1} for larger v. The MRD-CI and MRCI results generally agree within about 20 cm^{-1}, again usually smaller, though the MRCI results are as much as 50 cm^{-1} smaller at large v. However, the MRCI results compare significantly better than the MRD-CI for $v \leqslant 14$, while the reverse is true for larger v.

For the A-state rotational constants, the pseudopotential data again agree best, being within 0.025 cm^{-1}. The MRD-CI and MRCI values are again usually smaller by typically 0.05 cm^{-1}, though as much as 0.1 cm^{-1}. As for the X state, MRCI performs better at low v, while MRD-CI performs best at large v.

These comparisons show that, among the three potentials being considered here, in almost all cases the pseudopotential values [8] are the most accurate for the attractive regions of the potentials. For the X state the MRD-CI results are somewhat more accurate than the MRCI results [7], while the reverse is true for the A state. It should be emphasized that the deviations of both the MRD-CI [3] and the MRCI [7] well depths from the experimental data [17] (see Table I) are within about a factor of 2 of the pseudopotential ionic correction [8]. The absence of any adjustment and any smoothing for the MRD-CI and the MRCI potentials [3,7] results in deviations of vibrational spacings and rotational constants from the experimental data. Nevertheless, the MRD-CI and MRCI data [3,7] are used, where possible, in the present study for the dynamical treatment because they provide reliable nonadiabatic couplings, which is important because the low-energy inelastic cross sections between low-lying states are more sensitive to the couplings than to the potentials (see below).

For the X state the CCSD(T) calculations of [9] and the MRCI calculations of [16] are seen to be slightly more accurate than the pseudopotential calculation [8]. The influence of differences in the *ab initio* adiabatic potentials on the inelastic cross sections is shown and discussed in the next section. The data of [9] (see Fig. 1) are used in Sec. III B for trial adjustments of the MRD-CI [3] and the MRCI [7] potentials for the nuclear dynamics.

III. QUANTUM-DYNAMICAL CALCULATIONS

A. Nuclear-dynamical methods

The nuclear dynamics of Na + H collisions has been treated in the present study by means of two codes: (i) the one developed by Belyaev *et al.* [3,19] for solving the coupled-channel equations in the adiabatic or mixed adiabatic-diabatic representation and (ii) the code used in [8] for solving the coupled-channel equations in the diabatic representation. The former code handles cases with either zero [3] or nonzero [4,19,21] asymptotic couplings by means of the t-matrix method [19,21,26]. The mixed representation is constructed from the pseudopotential data in the adiabatic representation at $R < 40a_0$ and in the diabatic representation elsewhere. The latter code [8] is based on the code developed in [27] using the [28] version of the log-derivative method of [29] and requires asymptotic couplings to be zero.

Before proceeding further it is of interest to confirm that these two methods give identical results. Four-state results [3] solving in the adiabatic representation were compared with results using the technique from [13] to transform to a diabatic basis, followed by solution using the code of [8]. Results for the Na($3s \rightarrow 3p$) and Na($3s \rightarrow 4s$) excitation cross sections in collisions with H were compared for energies of 3–8 eV, and satisfactory agreement was obtained.

B. Near-threshold $3s \rightarrow 3p$ cross section and influence of different input data

Figure 5 shows the $3s \rightarrow 3p$ excitation cross section at collision energies within 0.04 eV of the threshold. These cross sections are based on hybrid potentials and couplings: X- and A-state potentials and the X-A radial coupling from the MRCI calculation [7], along with the B state $^1\Pi$ potential and the B-X and B-A rotational couplings from the MRD-CI calculation [3]. This energy range was previously studied using MRD-CI data [3].

Resonant structure is clearly seen due to orbiting resonances, predominantly in the A state (but possibly also in the B state). Similar resonances were found in [3] for the MRD-CI input data, but the positions and widths of the resonances are very sensitive to the adiabatic potentials, and so differ between the MRD-CI potential used in that work and the MRCI hybrid data used here. It is seen from Fig. 5 that the resonances are dense in energy and increase the cross section by up to six orders of magnitude compared to the very small ($\approx 10^{-8}$–10^{-7} Å^2) background cross section. In many cases the cross section reaches its unitarity limit for the single partial wave in which the resonance occurs. Nonadiabatic transition probabilities (not shown) in resonance cases are much larger than the typical value of 10^{-7} for background transition probabilities and can be up to 1 (e.g., for the kinetic energy $E = 2.13323$ eV and angular momentum quantum number $L = 46$ for the resonance), the cross section of which is shown in the inset of Fig. 5. For the resonances, L varies from ten to several hundreds. The widths of the resonances vary from 10^{-10} to 10^{-3} eV (see the inset in Fig. 5). Still narrower resonances may exist but are prohibitively expensive to find in a scattering calculation. We estimate the number of $3s \rightarrow 3p$ orbiting resonances with widths exceeding 10^{-10} eV to be around 500.

Very long-lived resonances will decay radiatively rather than by tunneling or vibronic coupling. We have estimated

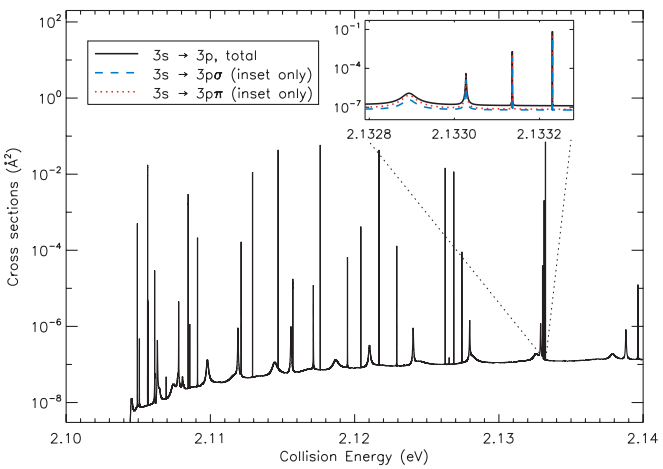

FIG. 5. (Color online) The resonant structure of the $3s \rightarrow 3p$ cross sections in the near-threshold energy range. The inset shows the orbiting resonances in the enlarged scale around $E = 2.133$ eV. The (red) dotted line in the inset is the $3s \rightarrow 3p\sigma$ partial cross section, the (blue) dashed curve is the $3s \rightarrow 3p\pi$ partial cross section, and the (black) solid line is the total $3s \rightarrow 3p$ excitation cross section. See text for the definition of the hybrid potentials and couplings used for the dynamical calculation.

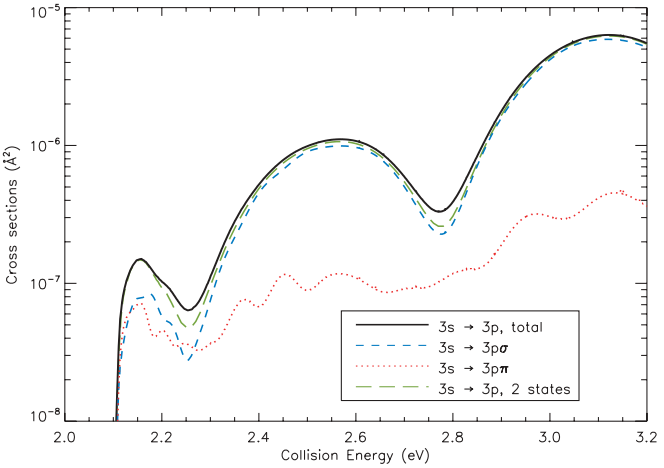

FIG. 6. (Color online) The background cross sections for $3s \rightarrow 3p$ excitation calculated using the X, A, and B states [the (black) solid, (red) dotted, and (blue) short-dashed lines are the same as in Fig. 5] and using only the X and A states [the (green) long-dashed line].

radiative lifetimes as being typically about 30 ns, based on results for the A state in LiH [30] and KH [31]. Hence, resonances narrower than 20 neV in width should be excluded from any average over a velocity distribution to obtain a rate coefficient. For astrophysical applications the rate coefficients are of interest, so we have performed test calculations, using a Maxwellian speed distribution, of the $3s \rightarrow 3p$ rate coefficients with and without the resonances to estimate the contribution of the orbiting resonances: roughly 25% at 2000 K, 15% at 5000 K, and 8% at 10 000 K.

The inset in Fig. 5 also clearly shows that, in the vicinity of the orbiting resonances, the $3s \rightarrow 3p\pi$ partial cross section (the dotted curve) exceeds the $3s \rightarrow 3p\sigma$ partial cross section (the dashed line). In the remaining discussion, the background cross sections, excluding the orbiting resonances, are mainly considered, keeping in mind the estimate for the contribution of the orbiting resonances to the rate coefficients.

The background $3s \rightarrow 3p$ excitation cross sections are shown in Fig. 6. The analysis shows that the $3s \rightarrow 3p\pi$ partial cross section exceeds the $3s \rightarrow 3p\sigma$ one only in two narrow energy regions, approximately 0.05 eV wide, below about 2.25 eV. The $3s \rightarrow 3p\sigma$ cross section shows Stückelberg oscillations, while the $3s \rightarrow 3p\pi$ cross section lacks such structure and increases with increasing energy more slowly than that for $3s \rightarrow 3p\sigma$. This means that at energies $E \gtrsim 2.3$ eV, except for a narrow range around 2.8 eV, excitation via the $B\,^1\Pi$ state can be neglected. Note that the positions of the orbiting resonances differ in the two- and in the three-channel treatment.

It is worth mentioning that the $3s \rightarrow 3p\sigma$ cross section in the two-state approximation does not coincide exactly with the $3s \rightarrow 3p\sigma$ partial cross section in the three-state treatment, yet the total cross sections are very similar (see Fig. 6). The reason is that, in the three-state treatment, nonadiabatic transitions from the $X\,^1\Sigma^+$ state mainly occur at internuclear distances $R < 10a_0$ into the $A\,^1\Sigma^+$ state, and the $B\,^1\Pi$ state is then populated basically from the outgoing current in the $A\,^1\Sigma^+$ state at large internuclear distances due to the rotational

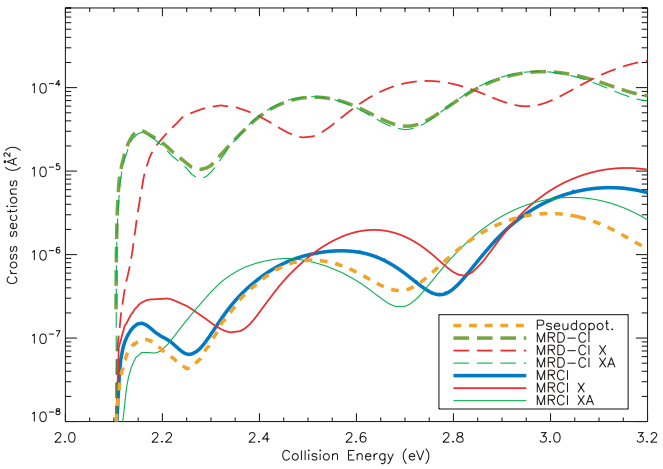

FIG. 7. (Color online) Comparison of the background cross sections for $3s \rightarrow 3p$ excitation calculated in the three-state approximation using different quantum-chemical data. The solid lines are the cross sections obtained with the MRCI data [7], the long-dashed lines are those using the MRD-CI data [3], and the short-dashed (orange) line is the cross section based on the pseudopotential data [8]. The B-state adiabatic potential and the rotational couplings with the X and A states are always taken from [3]. The additional label X means that the $X\,^1\Sigma^+$-state adiabatic potential is replaced by the corresponding potential from [9]. The label XA means that both the X and the $A\,^1\Sigma^+$-state adiabatic potentials are adjusted to the X-state potential from [9]. See the text for explanation of the adjustment.

coupling and asymptotic degeneracy between the A and B states. With increasing collision energy, the difference between the cross sections calculated in the two-state and the three-state treatments decreases and finally disappears. For this reason the main part of the dynamical calculations below is performed in the NaH($^1\Sigma^+$) system. The nonadiabatic transitions in the triplet NaH system lead to much smaller inelastic cross sections for this energy range, as shown in [3].

We now discuss the influence of different quantum-chemical data on the Na + H inelastic cross sections. The $3s \rightarrow 3p$ excitation cross sections calculated using the pseudopotential, the MRD-CI, and the MRCI input data are presented in Fig. 7. This figure also shows the results of the calculations with the X-state adiabatic potential, as well as both the X- and A-state potentials, replaced or adjusted using the CCSD(T) X-state potential from [9] (which is judged to be the most reliable and quite similar to the X-state pseudopotential; see Fig. 1). The A state is corrected by the same amount in absolute terms as the X state. More precisely, the X-state potential is replaced, while the A-state potential is adjusted so that the absolute difference between the original calculations of the X and A states at a given internuclear distance is retained.

It is seen in Fig. 7 that the pseudopotential data and the MRCI data provide cross sections of the same order of magnitude but with differing Stückelberg oscillations, while the MRD-CI input data yield cross sections two orders of magnitude larger.

We have found that the reason for these differences is rooted not in the differences in the potentials, but rather in the differences in the nonadiabatic couplings. Figure 7 shows that the replacement of the MRD-CI X-state potential with the X-state potential from [9], but keeping the same nonadiabatic radial coupling, changes the Stückelberg oscillations but gives the same order of magnitude for the cross section [the (red) long-dashed curve]. Adjustment of both the X-state and the A-state MRD-CI adiabatic potentials to the X-state potential for [9] results in the cross section [the thin (green) dashed line] practically coinciding with the cross section without any adjustment.

Similar results hold for the MRCI quantum-chemical data: adjusting one or two adiabatic potentials and keeping the same nonadiabatic couplings changes the cross-section oscillations but not the order of magnitude. It should be emphasized that the cross sections plotted in Fig. 7 are obtained in the three-channel treatment, but as mentioned earlier the two-channel approximation (the $^1\Sigma^+$ states only) gives the same cross sections except for the orbiting resonances and a narrow region just above the energy threshold. Thus, although the variation of adiabatic potentials changes the particular form of the energy dependence of the inelastic cross section, it keeps the order of magnitude, but differences in the nonadiabatic radial couplings may change the inelastic cross sections by several orders of magnitude. This conclusion agrees with that drawn in [7], where it has been found that using the same adiabatic potentials but slightly different radial couplings may change the inelastic cross section by orders of magnitude in the energy threshold region, and increasing the magnitude of the coupling may even provide a smaller cross section. At higher energies (not shown in Fig. 7; see [7]), the difference between the cross sections based on different input data decreases and at $E \gtrsim 5$ eV a larger coupling leads to larger cross sections, as commonly expected.

The analysis carried out in [7] by means of the perturbation approach and that in the present paper shows that this is the result of the particular form for the nonadiabatic coupling (see Fig. 2). A transition probability can be expressed via the integral of the radial coupling multiplied by the Wronskian of elastic wave functions [7]. At near-threshold energies, transition probabilities and cross sections are sensitive to even a small variation of the coupling—even more so to a change in sign—as the integrands are alternating functions and transition probabilities are small (see, e.g. Fig. 5 of [7]). Note that the LZ X-A radial coupling does not change sign, while all the calculated X-A couplings change sign, which finally results in high sensitivity of transition probabilities and cross sections to the particular shape of the coupling. It is seen in Fig. 2 that the MRD-CI and the MRCI X-A couplings are very similar; nevertheless, they lead to substantially different cross sections. The MRCI and the pseudopotential X-A couplings are different, but they lead to cross sections of the same order of magnitude. The fact that the cross sections based on the pseudopotential and the MRCI input data agree with each other and differ from those based on the MRD-CI data does not necessarily mean the former cross sections are more reliable. Rather, this just emphasizes that the excitation cross section is very sensitive to the nonadiabatic coupling.

For astrophysical applications, the inelastic rate coefficients are of interest. As an illustration, here we discuss the sensitivity to the different quantum-chemical data of the $3s \rightarrow 3p$ rate

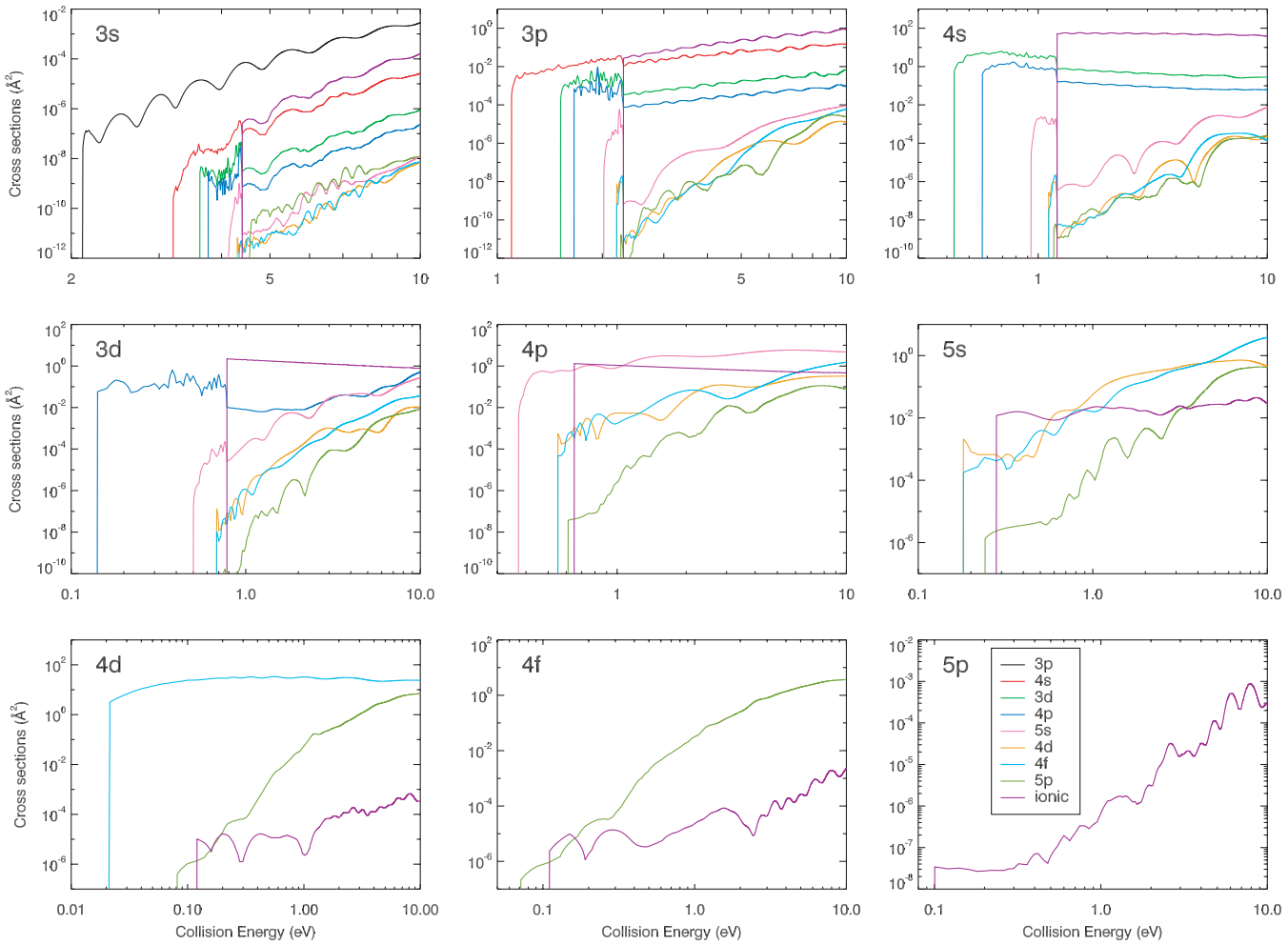

FIG. 8. (Color online) The cross sections for excitation processes calculated using the NaH $^1\Sigma^+$ pseudopotential data. The statistical probability factors have been included. The initial level is shown in each panel. The key is common to all panels and is shown in the bottom right ($5p$) panel. Note that the scales used in the various panels may differ.

coefficients for temperatures up to 10 000 K. We have found that the pseudopotential data (with the largest coupling) provide the lowest rate coefficients and the MRD-CI data (with the smallest coupling) yield the largest rate coefficients, greater than those using the pseudopotential data by factors of 116 at 2000 K, 74 at 5000 K, and 67 at 10 000 K. Rate-coefficient results for all the initial levels will be discussed in detail in a separate publication.

C. Cross-section overview

Excitation cross sections between the lowest ten $^1\Sigma^+$ states calculated using the pseudopotential diabatic data are presented in Fig. 8. De-excitation cross sections (omitted for clarity) can be inferred using detailed balance. All ten states have been included in the calculation, either as open or closed channels, depending on the energy. Collision energies from close to the first excitation threshold up to 10 eV are shown for each possible entrance channel. A logarithmic scale has been used to provide a clearer view of the lower energies more important for subsequent rate-coefficient calculations.

The cross sections shown have been calculated on an energy grid of 0.01 eV for energies on a $3s$ target between 2.11 and 3.0 eV, 0.02 eV between 3.0 and 4.8 eV, 0.05 eV between 4.8 and 10.0 eV, and 0.25 eV above 10.0 eV. In addition, a narrow region around 1.93 eV for entrance in the $3p$ channel was explored on a much finer grid and is discussed in the next section. While the coarser grid suffices to provide a good overview of the behavior of all the excitation cross sections, for some narrow energy regions, resonance structure occurs on a finer scale and will be explored more thoroughly for subsequent comprehensive rate-coefficient calculations to be published in the astrophysics literature.

The marked structure seen in practically all cross sections below the ionic threshold is discussed in the next section, particularly the examples of the $3p \rightarrow 3d$ and $4p$ cross sections. Among the other features of interest in the larger cross sections in Fig. 8, we note the following:

1. The $3s \rightarrow 3p$ cross section is the largest of the excitation cross sections from $3s$ and shows Stückelberg oscillations. Resonance structure at lower energies (not seen on this scale) is discussed in Sec. III B for the MRCI data and in Ref. [3] for

the MRD-CI data, and similar resonance structure occurs with the pseudopotential data.

2. The marked drop in the $3s \rightarrow 4s$ cross section at the opening of the ionic channel arises because the $4s$ channel is strongly coupled to the ionic channel near the threshold, consistent with the Na^+/H^- mutual neutralization being predominantly to $Na(4s) + H$ at low energies [8].

3. Below the ionic threshold, the largest excitation cross section from $3p$ is to $4s$, to which there is direct nonadiabatic coupling through the avoided crossings with the ionic state. As the avoided crossing is traversed more favorably than that for $3s$-$3p$, the cross section is significantly larger at comparable energies. With the opening of the ionic channel, the $4s$ cross section is largely converted to the ionic, as was discussed earlier for the $3s$ entrance channel. The $3p \rightarrow 3d$, $4p$ resonance structure is discussed in the following section.

4. Near the threshold the $4s \rightarrow 3d$ cross section is significantly larger than the $3p \rightarrow 4s$ cross section at comparable energies because the avoided crossing is more nearly diabatic. Above the ionic threshold the ionic channel dominates, for the reasons discussed earlier.

5. The $3d \rightarrow 4p$ cross section below about 1 eV shows considerable structure associated with the structure already seen in the $3p \rightarrow 3d$ and $4p$ cross sections. Again, because of the strong coupling with the ionic channel [8], that channel dominates above the ionic threshold.

6. In contrast to the $3p$, $4s$, and $3d$ entrance channels, the ionic channel does not dominate the $4p$ excitation cross sections, except for a narrow energy band immediately above the threshold. Instead, cross sections to the adjacent $5s$ excitation channel are dominant at almost all energies.

7. From the $5s$ and higher entrance channels the ionic-covalent avoided crossings are at such large distances as to be traversed diabatically. Hence, the primary coupling is at intermediate distances and is best seen as arising in the Fermi model describing a nearly free Na valence electron scattering elastically from the H atom [32]. Cross sections to the adjacent near-degenerate $4d$ and $4f$ levels are dominant at almost all energies.

8. It is seen from Fig. 8 that the largest cross section corresponds to the ion-pair ($Na^+ + H^-$) production from the $4s$ state. Among others, the following cross sections have large values: $4d \rightarrow 4f$, $4p \rightarrow 5s$, $4s \rightarrow 3d$ and $4p$, the ion-pair production from $3d$ and $4p$. Some cross sections have rather large values at relatively high energies (around 10 eV), for example, $3p \rightarrow 4s, 5s \rightarrow 4d, 4d \rightarrow 5p, 4f \rightarrow 5p, 4p \rightarrow 4d$ and $4f$, and $3d \rightarrow 4p$ and $5s$.

D. Feshbach resonances

As can be seen from Fig. 8, many resonances appear in the excitation cross sections for energies from excitation thresholds to the ionic threshold, in particular, in the $3p \rightarrow 3d$ and $4p$ cross sections for energies from the threshold to about 2.3 eV. Exploratory calculations have shown that these resonances are absent if closed channels are omitted from the calculation and consequently the resonances must be Feshbach resonances associated with temporary excitation and capture into a rovibrational level of a higher channel.

Such levels are also accessed spectroscopically as vibronic states where the quasibound state is sufficiently long lived for narrow spectral lines to be observed. Vibronic states in LiH have been studied in detail: of these the highest electronic state studied is the $D\,^1\Sigma^+$ [33]. There the calculated vibronic states had irregular vibrational spacings, typically about 70 cm^{-1}, and widths varying between 4×10^{-5} and 36 cm^{-1}. The spacings were comparable to those of the vibrational levels obtained in the $D\,^1\Sigma^+$ adiabatic state. As this attractive potential had an essentially ionic outer wall, the vibrational spacings were unusually small.

To obtain an estimate of the likely vibronic spacings for these NaH Feshbach resonances, the rovibrational levels of the sixth $^1\Sigma^+$ potential, dissociating to $Na(5s) + H$, have been investigated. This state, with an avoided crossing with the ionic state at $R \approx 73a_0$, has a double minimum (see Fig. 1) with a very wide attractive outer region, well depth of about 0.36 eV, and is largely ionic in character for $R \gtrsim 20a_0$. Using LEVEL [25], in this potential a high density of vibrational levels is found—about 140 rotationless vibrational states and almost 30 000 rovibrational levels, including over 5000 quasibound levels with energies up to about 0.12 eV above dissociation. Typical vibrational spacings are about 20 cm^{-1}. Obviously not all these rovibrational levels have angular momenta (maximum value 300 for the ground vibrational level) for which the avoided-crossing region is classically accessible at the related collision energy. Nevertheless a high density of levels which can give rise to Feshbach resonances is likely.

As an example of these resonances, we have scanned the region around 1.93 eV in the $3p$ entrance channel and cross sections are shown in Fig. 9. The cross sections around four resonances (two in each of the $3d$ and $4p$ channels) have been fitted to a constant background plus a Lorentzian of varying center, width, and height. As is clear from the figure, the resonances fit well to this form, although ideally the two close $4p$ resonances would be fitted simultaneously. The half widths at half maximum of the Lorentzians are in the range 0.05–0.1 cm^{-1}.

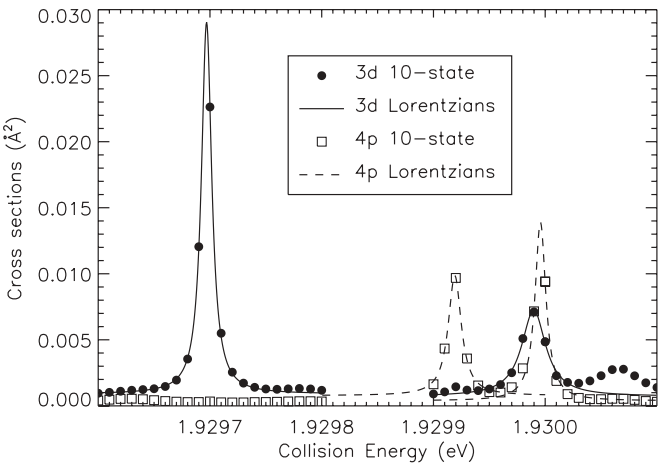

FIG. 9. The cross sections for $3p \rightarrow 3d$, $4p$ excitation calculated using the NaH $^1\Sigma^+$ pseudopotential data. Results of fits of Lorentzians to four of the resonances are also shown.

To explore this structure further, the $3p$-$3d$ and $3p$-$4p$ transition probabilities were investigated as a function of angular momentum L at a collision energy of 1.9362 eV (not shown). The probabilities for both final states showed marked peaks at $L = 29$ and 131, with some probabilities exceeding 0.1.

The present case may be more complicated than one of a Feshbach resonance associated with temporary capture into a single state, as there are many open and closed coupled states involved. Moreover, as mentioned earlier, at large distances $R \gtrsim 20a_0$, the system passes the avoided crossings diabatically, so temporary capture which is responsible for the Feshbach resonances occurs in the mixed state, which is ionic diabatic at large distances and mainly adiabatic (the C mixed with the A states) at short distances. For collisional energies exceeding the ionic threshold, the resonance structure disappears, as seen in Fig. 8. Such resonances must also occur in excitation of Li by H and may be important in other hydrogen-alkali-metal collisions.

IV. CONCLUSIONS

We have compared a number of different input quantum-chemical data sets from pseudopotential and *ab initio* calculations and their effects on excitation cross sections. Regarding the quantum chemistry input data, two particularly important results were found. First, the 2×2 diabatic potentials and the off-diagonal matrix element are substantially different from those of the 10×10 diabatic representation for the $3s$-$3p$ excitation. This is important, for example, in deriving LZ parameters. Second, the covalent $\mathrm{Na}(3s) + \mathrm{H}$ and $\mathrm{Na}(3p) + \mathrm{H}$ diabatic potentials cross at short distances, which results in deviation of the X-A radial coupling from the Lorentzian coupling, including a change of sign, at short distances. Regarding cross sections, the near-threshold cross section for the $3s$-$3p$ excitation was found to vary dramatically depending on the input radial coupling data between these two states. The variation is not what might be naively expected; large differences in the height and width of the radial coupling do not translate directly into large differences in cross sections. In fact, the two radial coupling data sets that are most similar, MRD-CI and MRCI, show the largest differences, around two orders of magnitude near the threshold.

An extensive set of cross sections between the ten lowest levels, including the ionic channel, up to collision energies of 10 eV were calculated. The cross sections show a large variation in amplitude for different transitions, from as large as 50 to as small as 10^{-12} Å^2. The $3s$-$3p$ cross sections show orbiting resonances, which have been seen in earlier studies, and Feshbach resonances associated with closed channels are also found to be present in the low-energy cross sections for some transitions. It is clear that the cross sections are of varying precision. From the preceding discussion, it is clear that the $3s$-$3p$ near-threshold cross section is uncertain by two orders of magnitude. However, this case is expected to have the largest uncertainty. Since the X-A energy splitting at the avoided ionic crossing is the largest of such crossings, and the nonadiabatic transition probabilities in this particular nonadiabatic region are very small at the energy threshold, this leads to the $3s$-$3p$ transition probabilities and cross sections having the greatest near-threshold sensitivity to the radial coupling input data. This sensitivity becomes smaller with increasing collision energy as the transition probabilities become larger. Although this nonadiabatic region is involved in other transitions, for example, $3s$-$4s$, the collision energies are naturally larger when the system passes this nonadiabatic region and the uncertainties are reduced. Calculations for $3s$-$4s$ indicate that the uncertainty is only around one order of magnitude at the threshold, a factor of 10 less than for $3s$-$3p$. For other transitions, we expect the uncertainties to be even smaller—certainly better than an order of magnitude, and perhaps as good as a factor of 2.

These calculations are expected to be of sufficient precision to evaluate their astrophysical importance, and certainly far more reliable than the often-used so-called Drawin formula (see [1]), a formula based on several modifications of Thomson's classical estimate for ionization by electrons. It should also be noted that the Drawin formula only provides estimates for optically allowed transitions. As mentioned, rate coefficients for astrophysical application will be presented in the astrophysical literature, and comparison with the Drawin formula will be made and the data included in astrophysical modeling. Initial comparisons show differences of many orders of magnitude with a large scatter compared to the Drawin formula, as was found for $\mathrm{Li} + \mathrm{H}$ [6].

ACKNOWLEDGMENTS

We gratefully acknowledge the support of the Royal Swedish Academy of Sciences, Göran Gustafssons Stiftelse, and the Swedish Research Council. P.S.B. is supported by a grant from the Knut and Alice Wallenberg Foundation. A.K.B. gratefully acknowledges the support from the Russian Foundation for Basic Research (Grant No. 08-03-00928-a) and from the Max-Planck-Institute for Astrophysics (Garching, Germany).

[1] W. Steenbock and H. Holweger, Astron. Astrophys. **130**, 319 (1984).

[2] I. Fleck, J. Grosser, A. Schnecke, W. Steen, and H. Voigt, J. Phys. B **24**, 4017 (1991).

[3] A. K. Belyaev, J. Grosser, J. Hahne, and T. Menzel, Phys. Rev. A **60**, 2151 (1999).

[4] A. K. Belyaev and P. S. Barklem, Phys. Rev. A **68**, 062703 (2003).

[5] H. Croft, A. S. Dickinson, and F. X. Gadéa, J. Phys. B **32**, 81 (1999).

[6] P. S. Barklem, A. K. Belyaev, and M. Asplund, Astron. Astrophys. **409**, L1 (2003).

[7] A. K. Belyaev, Eur. Phys. J. D **44**, 497 (2007).
[8] A. S. Dickinson, R. Poteau, and F. X. Gadéa, J. Phys. B **32**, 5451 (1999).
[9] B. K. Taylor and P. R. Newman, J. Chem. Phys. **118**, 8770 (2003).
[10] F. X. Gadéa and M. Pélissier, J. Chem. Phys. **93**, 545 (1990).
[11] T. Romero, A. Aguilar, and F. X. Gadéa, J. Chem. Phys. **110**, 6219 (1999).
[12] F. X. Gadéa and A. Boutalib, J. Phys. B **26**, 61 (1993).
[13] F. T. Smith, Phys. Rev. **179**, 111 (1969).
[14] R. J. Buenker, S. D. Pyermihoff, and W. Butscher, Mol. Phys. **35**, 771 (1978).
[15] P. J. Bruna and S. D. Peryerimhoff, Adv. Chem. Phys. **67**, 1 (1987).
[16] C.-L. Yang, X. Zhang, and K.-L. Han, J. Mol. Struct., Theochem **676**, 209 (2004).
[17] W. C. Stwalley, W. T. Zemke, and S. C. Yang, J. Phys. Chem. Ref. Data **20**, 153(1991).
[18] L. F. Errea, L. Méndez, O. Mó, and A. Riera, J. Chem. Phys. **84**, 147 (1986).
[19] J. Grosser, T. Menzel, and A. K. Belyaev, Phys. Rev. A **59**, 1309 (1999).
[20] A. Macías and A. Riera, Phys. Rep. **90**, 299 (1982).
[21] A. K. Belyaev, D. Egorova, J. Grosser, and T. Menzel, Phys. Rev. A **64**, 052701 (2001).
[22] A. K. Belyaev, A. Dalgarno, and R. McCarroll, J. Chem. Phys. **116**, 5395 (2002).
[23] F. P. Pesl, S. Lutz, and K. Bergmann, Eur. Phys. J. D **10**, 247 (2000).
[24] M. Rafi, N. Ali, K. Ahmad, I. A. Khan, M. A. Baig, and Z. Iqbal, J. Phys. B **26**, L129 (1993).
[25] R. J. Le Roy, University of Waterloo, Waterloo, Ontario, Canada, Tech. Rep. CP-663, 2007 (unpublished).
[26] A. K. Belyaev, Phys. Scr. **80**, 048113 (2009).
[27] R. J. Allan and H. J. Korsch, Z. Phys. A **320**, 191 (1985).
[28] D. E. Manolopoulos, J. Chem. Phys. **85**, 6425 (1986).
[29] B. R. Johnson, J. Comp. Phys. **13**, 445 (1973).
[30] F. X. Gadéa, H. Berriche, O. Roncero, P. Villareal, and G. Delgado Barrio, J. Chem. Phys. **107**, 10515 (1997).
[31] N. Khelifi, B. Oujia, and F. X. Gadéa, J. Russ. Laser Res. **27**, 575 (2006).
[32] A. S. Dickinson and F. X. Gadéa, J. Mol. Struct., Theochem **621**, 87 (2003).
[33] C.-Y. Wu, W.-T. Luh, F. X. Gadéa, and W. C. Stwalley, J. Chem. Phys. **128**, 064303 (2008).